communications materials

A Nature Portfolio journal

Article

https://doi.org/10.1038/s43246-026-01081-5

Discovery of magnetic-field-tunable density modulations and spin tilting in a layered altermagnet

Christopher Candelora[1], Muxian Xu[1], Siyu Cheng[1], Alessandro De Vita[2,3], Davide Romanin[4], Chiara Bigi[5], My Bang Petersen[6], Alexander LaFleur[1], Wilber Alfaro Castro[1], Federico Motti[7], Pasquale Orgiani[7,8], Giovanni Vinai[7], Matteo Calandra[9], Jill Miwa[6], Younghun Hwang[10] ✉, Ziqiang Wang[1], Federico Mazzola[11,12] ✉ & Ilija Zeljkovic[1] ✉

Altermagnets recently emerged as a new class of magnetic materials, arising from specific spin crystal symmetries. They exhibit a spin-polarized electronic band structure similar to ferromagnets, yet possess zero net magnetization, promising exotic properties. Here we study a layered triangular lattice altermagnet, cobalt-intercalated $NbSe_2$ using scanning tunneling microscopy and spectroscopy (STM/S). Spectroscopic-imaging STM and spin-polarized STM reveals emergent $2a_0$ tri-directional charge and spin density modulations on the selenium surface. Density functional theory simulations suggest these modulations reflect the underlying cobalt superstructure. We discover that an out-of-plane magnetic field tunes the modulation amplitudes and the electronic density-of-states in a manner dependent on the field direction and strength. This behavior is attributed to the field-induced tilting of cobalt spins, which can have profound implications on the electronic properties of the altermagnet. Our results provide atomic-scale insights to uncover a magnetic-field tunable altermagnetic band structure, highlight the importance of understanding spin canting in altermagnets.

For decades, the field of magnetism has focused on classifying collinear magnetic orders into two main categories: antiferromagnetic orders or ferromagnetic orders. The former is a crystal-symmetry compensated state with a net zero magnetization and Kramers degenerate bands, while the latter arises from spin splitting of the electronic band structure, generating a net magnetization. In recent years, several groups reported theoretical predictions of collinear antiferromagnets demonstrating various time-reversal symmetry breaking phenomena and spin-polarized behaviors[1–4], subsequently named altermagnets[5]. Altermagnetism exists in the space between antiferromagnetism and ferromagnetism—it is characterized by a net zero magnetization, yet the Kramers degeneracy is lifted by a non-relativistic, momentum-dependent spin-splitting of the electronic bands. The band splitting is driven by crystal symmetries connecting opposite-spin sublattices, linked by rotational symmetry in real space[6]. Due to intrinsic time-reversal symmetry breaking predicted to emerge in these systems, altermagnets have been theorized to exhibit numerous exotic phenomena, such as large anomalous Hall effect, spin-polarized currents and magneto-optical Kerr effect[2,7,8].

Since its initial theoretical formulation, altermagnetism and related properties have now been explored in several materials, such as RuO_2[9–21], MnTe[22–29] and others[30–36]. MnTe for example has been found to exhibit Kramers degeneracy lifting[22–24], an anomalous Hall effect[25,26], anisotropic magnetoresistance[27] and time-reversal symmetry breaking[28]. As altermagnetism is generally driven by specific crystal symmetries of the spin-sublattice, it is crucial to fully understand the spin ordering in these systems, whether other strongly correlated electronic phases can be realized, and to what extent spins can be tuned by external parameters. This has, however, remained challenging. Moreover,

---

[1]Department of Physics, Boston College, Chestnut Hill, MA, USA. [2]Institut für Physik und Astronomie, Technische Universität Berlin, Berlin, Germany. [3]Fritz Haber Institut der Max Planck Gesellshaft, Berlin, Germany. [4]Centre de Nanosciences et de Nanotechnologies, CNRS, Université Paris-Saclay, 10 Boulevard Thomas Gobert, Palaiseau, 91120, France. [5]Synchrotron SOLEIL, Saint-Aubin, France. [6]Department of Physics and Astronomy, Interdisciplinary Nanoscience Center, Aarhus University, Aarhus C, Denmark. [7]CNR - Istituto Officina dei Materiali (IOM), Trieste, Italy. [8]AREA Science Park, Trieste, Italy. [9]Department of Physics, University of Trento, Via Sommarive 14, 38123, Povo, Italy. [10]Electricity and Electronics and Semiconductor Applications, Ulsan College, Ulsan, Republic of Korea. [11]CNR-SPIN, Napoli, Italy. [12]Department of Physics and Astronomy ‘Galileo Galilei’, University of Padova, Padova, Italy. ✉e-mail: younghh@uc.ac.kr; federico.mazzola@spin.cnr.it; ilija.zeljkovic@bc.edu

there has been little atomic-scale insights exploring the family of altermagnets.

Recently, a quasi-2D layered system, Co-intercalated 2*H*-NbSe$_2$ (Co$_{0.25}$NbSe$_2$), emerged as another altermagnetic candidate[37]. Experiments, supported by theoretical calculations, showed that it exhibits a spin-polarized electronic band structure consistent with altermagnetism[37–39]. Given that the “parent” material 2*H*-NbSe$_2$ hosts the canonical $3a_0 \times 3a_0$ charge density wave and superconductivity[40–42], Co intercalation of the superconducting 2*H*-NbSe$_2$ is a potentially promising platform in the quest for engineering correlated electron states that coexist with altermagnetism. Indeed, through optical pump-and-probe spectroscopy as well as magnetic susceptibility measurements, two phase transition temperatures have already been identified, one around 150 K which has been attributed to the altermagnetic transition, and another around 50 K which has yet to be fully characterized, suggesting a richer electronic environment beyond pure altermagnetism[37,39]. In this work, we study altermagnet Co$_{0.25}$NbSe$_2$ using a combination of low-temperature spectroscopic imaging STM, spin-polarized STM, and density functional theory (DFT) to provide a fresh insight into this newly fabricated system. We observe non-dispersive $2a_0 \times 2a_0$ charge modulations on the Se termination, distinct from those in the parent compound 2*H*-NbSe$_2$. DFT surprisingly confirms a $2a_0 \times 2a_0$ charge modulation on the Se termination, suggesting that the Se surface can serve as a “window" into the Co superstructure underneath, allowing us to probe the magnetic ordering. Although DFT simulations agree well with the measured topographs, differential conductance d*I*/d*V* spectra further reveal a partial gap opening centered at the Fermi level, which is not observed in our DFT calculations of the material in the altermagnetic state, possibly suggesting an origin beyond pure altermagnetic state with spins perfectly aligned with the *c*-axis. By performing spin-polarized STM, we detect a spectroscopic change in the density of states (DOS), accompanied by a change in the relative intensities of the charge modulations for different STM tip-spin direction. This measurement suggests an additional spin component associated with the modulations. Interestingly, we find that the out-of-plane magnetic field can be used to alter the electronic density-of-states, as well as the amplitude of density wave modulations, which can gradually increase or decrease depending on the direction and strength of the magnetic field. Taken together, our experiments reveal an apparent tunability that can be attributed to Co spins that are not fully aligned with the *c*-axis, being tilted by the external magnetic field, which can have profound implications on the altermagnetic properties and should be taken into account to fully understand this system and related altermagnets.

Results

Surface characterization and identification of charge modulations

We cleave the samples in ultra-high vacuum at cryogenic temperature and immediately insert them into the microscope head (“Methods”). The crystals have a 2D layered structure, with interstitial Co atoms residing between adjacent Se-Nb-Se slabs, above the Nb atoms (Fig. 1a). The topographic height between adjacent layers is 6.2 Å (Fig. 1b), which matches the expected interlayer distance extracted from the diffraction measurements (Fig. 1a). Typical STM topographs show a hexagonal lattice with two possible surface terminations: the Se termination in which Se atoms form a hexagonal lattice with the lattice constant $a_0 \approx 3.7$ Å (Fig. 1c), or the Co

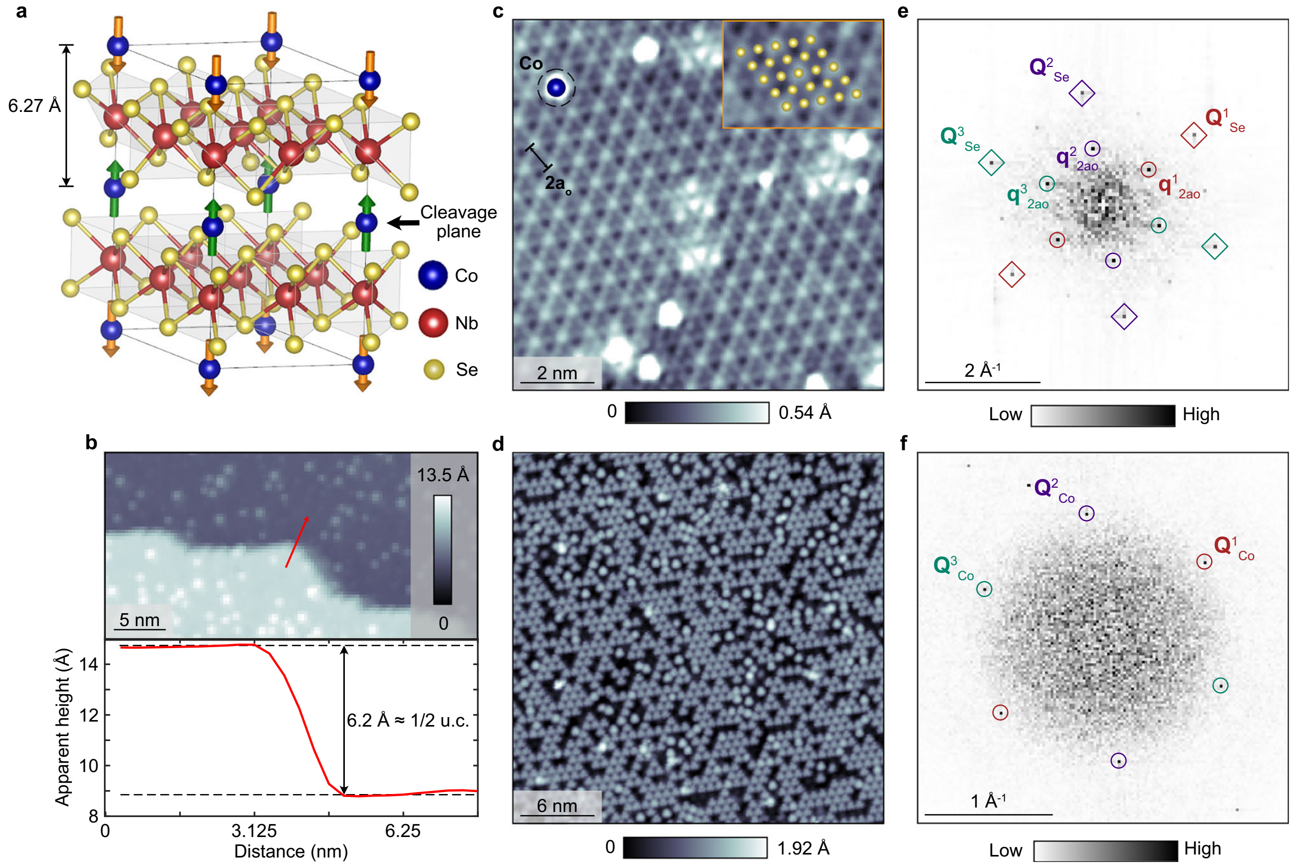

Fig. 1 | Crystal structure and surface identification. **a** 3D ball model of the crystal structure of Co$_{0.25}$NbSe$_2$ as viewed from the side. **b** (Top) STM topograph of a step edge from a Se-termination to the next Se-termination. (Bottom) A linecut perpendicular to the step-edge along the red line in the top panel, smoothed by the nearest-neighbor averaging. The step height is approximately a half the unit cell shown in (**a**). **c**, **d** STM topographs of the Se-terminated surface and the Co superstructure, respectively. **e**, **f** Drift-corrected Fourier transforms of the Se surface and Co surface in (**c**, **d**), respectively. Circles denote the peaks corresponding to a real-space wave length of $2a_0$, while the diamonds corresponds to the a_0 wave length. STM setup conditions: **b** $V_{\mathrm{sample}} = 1$ V, $I_{\mathrm{set}} =$ 10 pA; **c**, $V_{\mathrm{sample}} = 50$ mV, $I_{\mathrm{set}} = 200$ pA; **d** $V_{\mathrm{sample}} = 100$ mV, $I_{\mathrm{set}} =$ 10 pA.

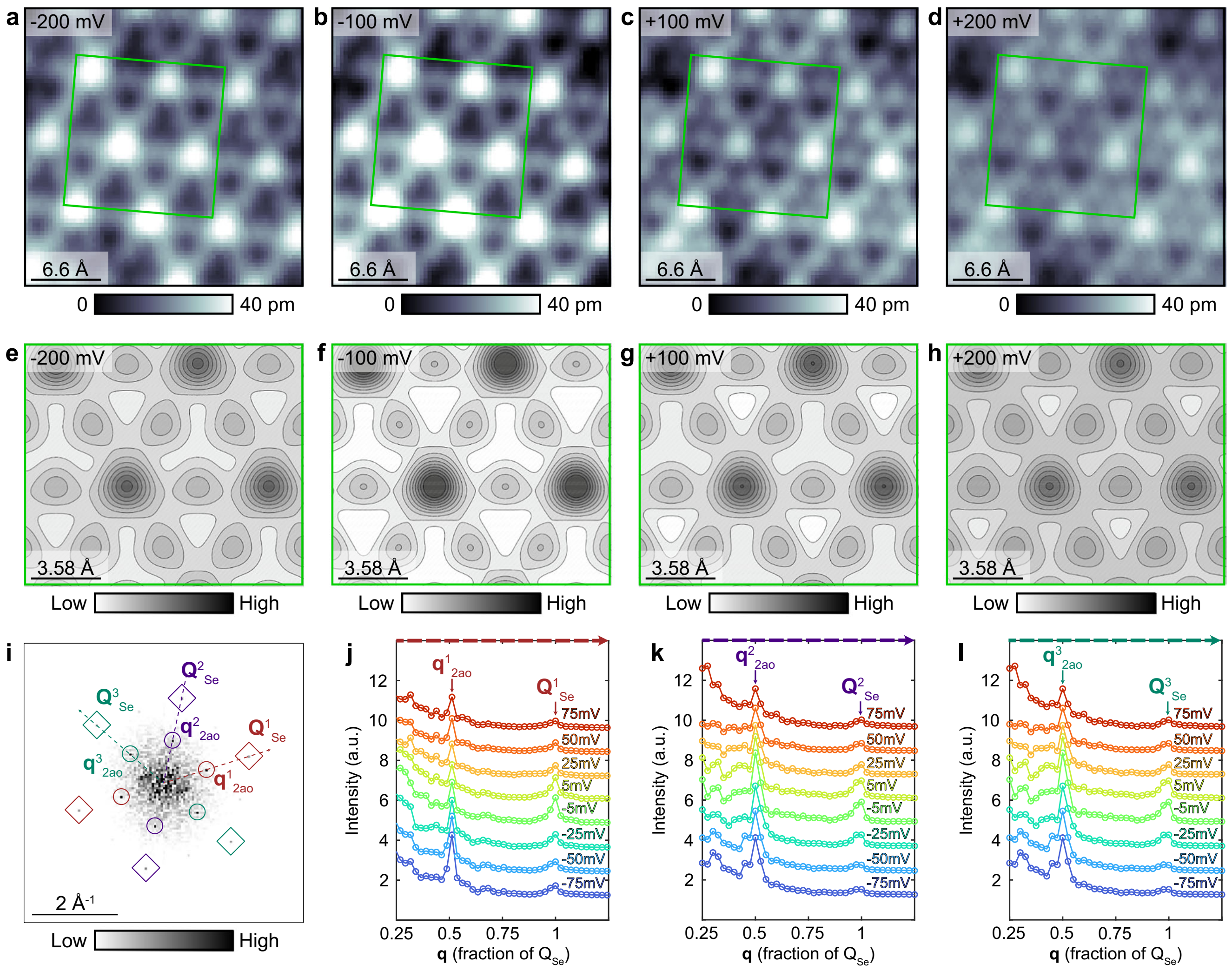

Fig. 2 | Energy dependence of charge modulations. **a–d** Bias dependent STM topographs of the Se surface. **e–h** DFT simulations of the Se termination with a constant tip height of 3 Å (see "Methods"). **i** A representative Fourier Transform of the Se termination. **j** Linecut taken along $\mathbf{Q}^1_{Se}$ as defined by red dotted line in (**i**) for different biases, with $\mathbf{q}^1_{2ao}$ and $\mathbf{Q}^1_{Se}$ identified. **k, l** Same as (**j**) but taken along $\mathbf{Q}^2_{Se}$ and $\mathbf{Q}^3_{Se}$, respectively. STM setup conditions: **a** $V_{\text{sample}} = -200$ mV, $I_{\text{set}} = 100$ pA; **b** $V_{\text{sample}} = -100$ mV, $I_{\text{set}} = 100$ pA; **c** $V_{\text{sample}} = 100$ mV, $I_{\text{set}} = 100$ pA.**d** $V_{\text{sample}} = 200$ mV, $I_{\text{set}} = 100$ pA.

termination where some of the interstitial Co atoms are left on top of the Se surface (Fig. 1d, and Supplementary Fig. 8). The remaining Co atoms on the surface exhibit a tendency to order into a 2 × 2 superstructure, consistent with their expected structure in the bulk between the adjacent NbSe_2 slabs[37]. Interestingly, STM topographs of the Se termination also show additional modulations that are approximately commensurate with the Se lattice, where every other atom appears brighter than the adjacent ones in all in-plane lattice directions (inset in Fig. 1c). This can be seen in the corresponding Fourier transforms (FTs) of STM topographs where, in addition to the Se atomic Bragg peaks, another set of superstructure peaks with wave vectors $\mathbf{q}^i_{2a0} = \frac{1}{2}\mathbf{Q}^i_{Se}$ (i = 1, 2, or 3 labels different in-plane lattice direction) appears (Fig. 1e). We have observed these 2 × 2 modulations on 5 samples with 8 different STM tips. The $3a_0 \times 3a_0$ charge density wave state known to exist in the bulk and on the Se surface of undoped NbSe_2 at about $\frac{1}{3}\mathbf{Q}^i_{Se}$[40] is notably absent in $\text{Co}_{0.25}\text{NbSe}_2$ (Fig. 1e, f). The $2a_0 \times 2a_0$ modulations detected on the Se surface are centered directly on top of Se atoms (Fig. 1c). This is laterally offset from the Co atom positions, which are centered under every other Nb atom in the layer below (Fig. 1a).

In this work, we primarily focus on characterizing the Se surface termination. To gain further insight into the observed charge modulations, we acquire a series of STM topographs and differential conductance $\mathrm{d}I/\mathrm{d}V(\mathbf{r},V)$ maps in a range of biases (Fig. 2, and Supplementary Fig. 1). The same $\mathbf{Q}^i_{2a0} = \frac{1}{2}\mathbf{Q}^i_{Se}$ peaks can be seen by eye and in the FTs of all STM topographs acquired with a bias between −500 and +500 meV (Fig. 2a–d, i, and Supplementary Figs. 1–3). Similarly, $\mathbf{Q}^i_{2a0}$ is detected in $\mathrm{d}I/\mathrm{d}V(\mathbf{r}, V)$ in a range of different biases (Supplementary Fig. 1g–i). The wave vectors are extremely localized in reciprocal space (~1–2 pixels width or 0.007–0.014 Å^{-1} width) and non-dispersive with energy. To determine the precise origin of these charge modulations, we turn to DFT calculations ("Methods"). Topographic simulations at −200 mV, −100 mV, +100 mV, and +200 mV capture most features seen in experiment, including the $2a_0 \times 2a_0$ modulation (Fig. 2e–h). The $2a_0 \times 2a_0$ structure seen is a projection of the Co electronic superstructure to the surface, allowing us to probe this otherwise inaccessible layer. The $2a_0 \times 2a_0$ charge modulations remain visible in STM data up to at least 50 K, which was the highest temperature scale accessible in our STM experiment (Supplementary Fig. 4).

Spin-polarized sample characterization and effects of magnetic field

Using the Se termination as a "window" to the underlying Co superstructure, it is interesting to further examine if there are any detectable spin characteristics associated with the charge modulations to see if spin information is also transmitted to the surface. For this purpose, we utilize spin-polarized STM tips such that the spin polarization of the tip can be controlled by external magnetic field (Supplementary Fig. 6, “Methods”). We acquire topographs and d*I*/d*V*(**r**, *V*) maps (Fig. 3a, b, and Supplementary Fig. 5) as a function of magnetic field applied parallel or antiparallel to the *c*-axis. By subtracting d*I*/d*V* maps taken over identical areas at different fields to create a spin-resolved magnetic contrast map (M(**r**, *V*)) (Fig. 3c), we are able to visualize in real space a $2a_0 \times 2a_0$ spin modulation commensurate with the charge. Let us first focus on the intensity of the three $|\mathbf{Q}^i_{2a0}|$ peaks in STM topographs acquired in magnetic field applied in the opposite directions (Fig. 3e). We can observe systematic differences in the intensities for positive magnetic fields, when the tip spin polarization is “up”, compared to negative magnetic fields when the tip’s spin polarization is “down” (Fig. 3e). Examining this behavior in more detail, a similar asymmetry can be seen in FTs of d*I*/d*V*(**r**,*V*) maps as well. Dispersions of the intensities of $|\mathbf{Q}^i_{2a0}|$ as a function of bias *V* (Fig. 3f–h), as well the d*I*/d*V* spectrum (Fig. 3i), appear distinctly different for opposite directions of the magnetic field. The change is systematic across many fields swept and different bias setup conditions used (Fig. 4, and Supplementary Fig. 7).

Given the strong agreement between theory and DFT in topographs, it is interesting to further compare these experimental spectroscopic features to theory. A notable difference between the integrated DOS spectrum from surface-projected DFT calculations and our large-scale STM d*I*/d*V* spectrum is that DFT predicts no prominent spectral gap at the Fermi level in the altermagnetic state of the system (Fig. 3i, j). However, our d*I*/d*V* spectra detect a partial V-shaped spectral gap $\Delta \approx 30$ meV centered at the Fermi level (Fig. 3i). Thus, some qualitative difference must be present between the DFT optimized structure and STM experiments. We find that the gap is

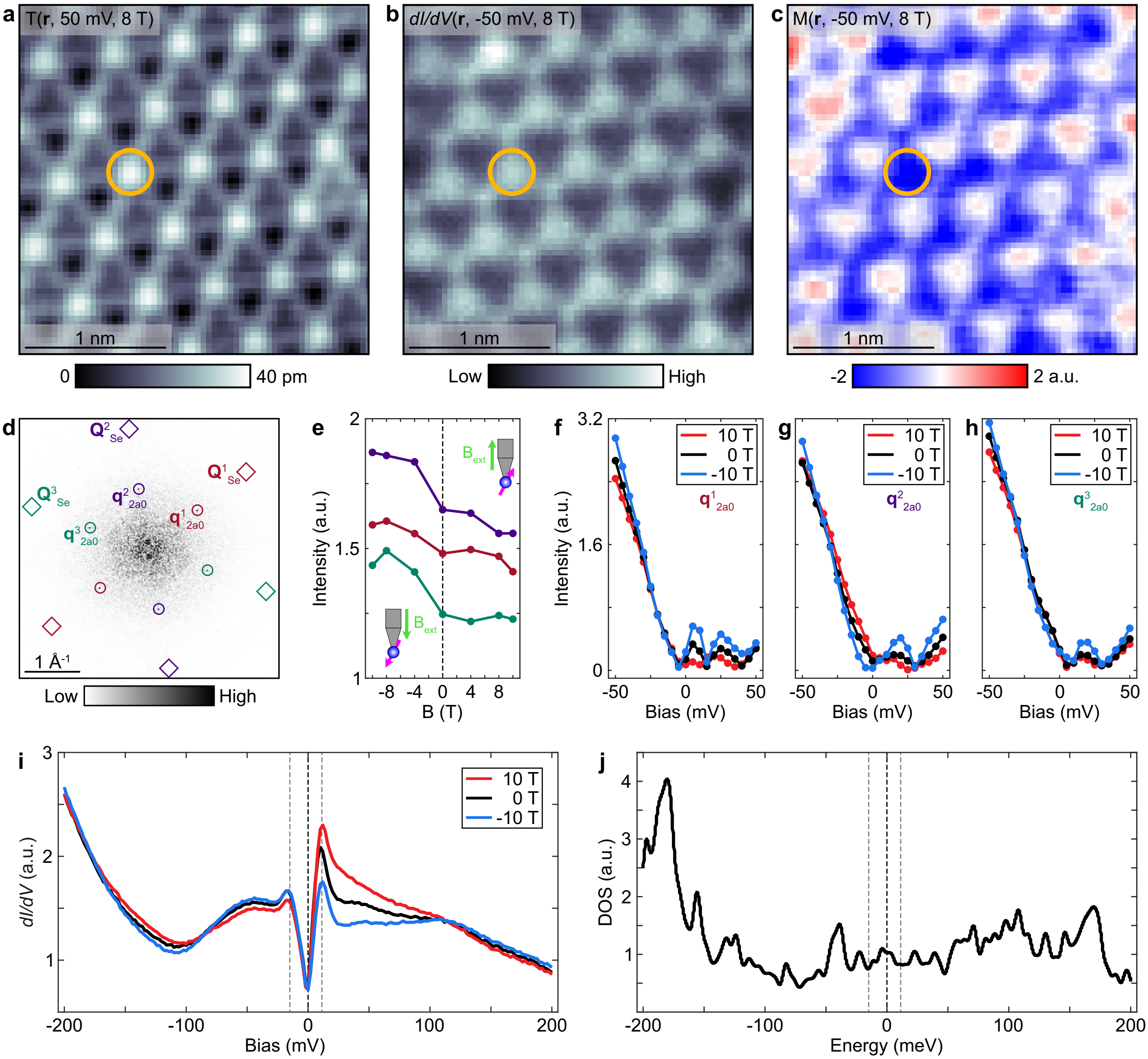

Fig. 3 | Characterization of spin modulations using spin-polarized STM. a Drift-corrected STM topograph at 8 T, **b** *dI/dV* layer from a DOS map of the same area, and **c** Spin-resolved magnetic contrast map *M*(**r**) obtained by subtracting the *dI/dV* map in **b** from its −8 T counterpart. **d** Fourier transform of the area shown in Supplementary Fig. 5, which was the area used to obtain data in **e**–**i**. **e** Intensities of the three charge modulation peaks from the Fourier transform of STM topographs taken at different fields with a spin-polarized tip. Inset cartoon schematics show spin-polarized tip alignment with external magnetic field. **f**–**h** Intensities of the charge modulation peaks $\mathbf{q}^1_{2a0}$, $\mathbf{q}^2_{2a0}$, and $\mathbf{q}^3_{2a0}$ in d*I*/d*V* maps as a function of energy for different magnetic fields. **i** d*I*/d*V* spectra of the Se surface at 0 T (black), 10 T (red), and −10 T (blue) taken over the area denoted by a yellow square in Supplementary Fig. 5. **j** DFT-simulation of the Se-projected density of states summed over the Se surface atoms from a simulation of the Se-terminated surface. STM setup conditions: **a** $V_{sample} = 50$ mV, $I_{set} = 200$; **b** $V_{sample} = 50$ mV, $I_{set} = 200$, $V_{exc} = 5$ mV (rms); **e**–**h** $V_{sample} = 50$ mV, $I_{set} = 150$ pA, $V_{exc} = 5$ mV (rms); **i** $V_{sample} = -200$ mV, $I_{set} = 200$ pA, $V_{exc} = 2$ mV (rms).

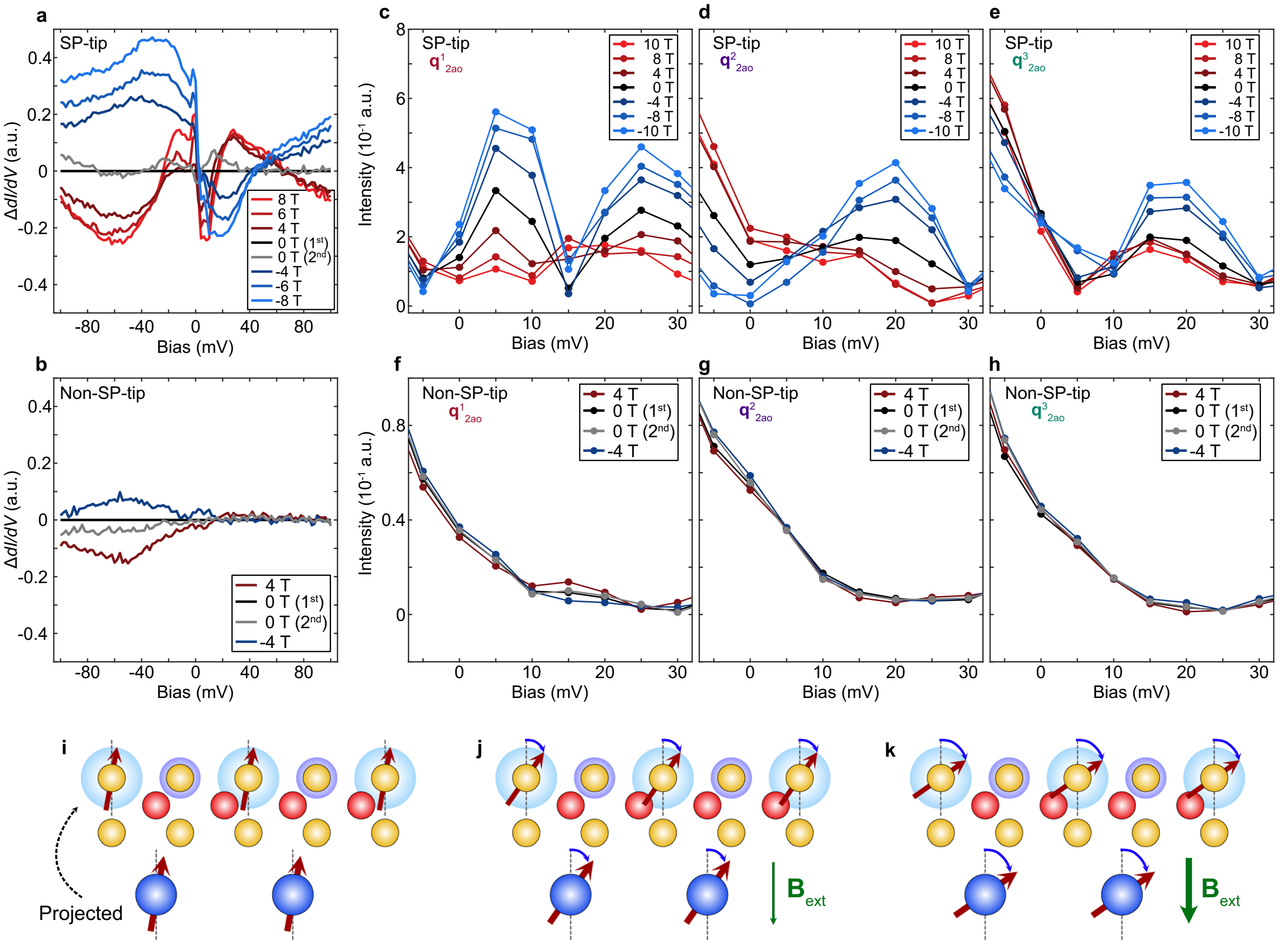

Fig. 4 | Magnetic tunability of the electronic density-of-states and the density wave modulations. a Difference in spectra ($\Delta(dI/dV)$) defined as the spectrum at some field subtracted from the first 0 T measurement taken ($dI/dV(B_z) - dI/dV(0T\,(1^{st}))$). Spectra were acquired with a spin-polarized tip. **b** Same as (**a**), but with data acquired with a non-spin-polarized tip. **c**–**e** Intensity of the $2a_0$ peaks in Fourier space as a function of sample bias for different magnetic fields along $\mathbf{q}^1_{2a0}$, $\mathbf{q}^2_{2a0}$, and $\mathbf{q}^3_{2a0}$, respectively acquired with a spin-polarized tip. **f**-**h**, The same as (**c**–**e**), but with data acquired with a non-spin-polarized tip. A pedagogical cartoon demonstrating a possible spin-canting scenario in **i** no field, **j** weak field, **k** stronger field to explain the behavior seen in (**c**–**e**). STM setup conditions: **a** $V_{\mathrm{sample}} = 100$ mV, $I_{\mathrm{set}} = 300$ pA, $V_{\mathrm{exc}} = 2$ mV (rms); **b** $V_{\mathrm{sample}} = 100$ mV, $I_{\mathrm{set}} = 300$ pA, $V_{\mathrm{exc}} = 2$ mV (rms); **c**–**e** $V_{\mathrm{sample}} = 50$ mV, $I_{\mathrm{set}} = 150$ pA, $V_{\mathrm{exc}} = 5$ mV (rms); **f**–**h** $V_{\mathrm{sample}} = 50$ mV, $I_{\mathrm{set}} = 150$ pA, $V_{\mathrm{exc}} = 5$ mV (rms).

generally homogeneous across the sample and impurities (Supplementary Fig. 12). The spectra show a substantial amount of residual conductance at zero energy (Fig. 3i, and Supplementary Fig. 12), suggesting that the Fermi surface is not fully gapped at low temperature.

Lastly, we turn to the most intriguing aspect of our spin-polarized STM data. As we examine the evolution of dI/dV spectra more closely, we observe a continuous change in the intensity at higher magnetic fields (Fig. 4a). $|\mathbf{Q}^i_{2a0}|$ Fourier transform amplitudes also exhibit fine magnetic-field-induced changes at higher fields (Fig. 4c–e, and Supplementary Fig. 9). These cannot be explained by a gradual change of the STM tip polarization direction only, as the tip's spin-direction should already be fully aligned with the external field by a few Tesla. As such, it appears that out-of-plane magnetic field modifies the electronic density-of-states of the sample as well as the spin modulations associated with the Co superstructure. To better understand if these magnetic-field-induced changes concomitantly alter electronic properties in the pure charge channel, we repeat equivalent measurements with a non-spin-polarized STM tip. Interestingly, we find a smaller, but nevertheless sizable, response in the electronic density-of-states, resulting in a spectral change of opposite magnitude when magnetic field reverses direction (Fig. 4b). The amplitudes of $|\mathbf{Q}^i_{2a0}|$ show substantially smaller changes as a function of the fields taken compared to the spin-polarized data (Fig. 4f–h, and Supplementary Fig. 10). Given that the spin-polarized tunneling current is proportional to the alignment between the tip and sample ($I_{SP} \propto \vec{P}_S \cdot \vec{P}_t$), we can only attribute this to a gradual "canting" of the Co spins with a pronounced effect on the electronic density-of-states. Fig. 4i–k shows a simple cartoon schematic of this gradual "canting" behavior, consistent with our experimental data.

Discussion

While the field of altermagnetism has progressed rapidly, atomic-scale imaging of material candidates has been extremely rare. Our experiments provide an atomic-scale spectroscopic glimpse to reveal $2a_0 \times 2a_0$ modulations with both charge and spin components in Co-intercalated NbSe$_2$. Based on DFT simulations, we attribute these modulations to the reflection of the ordering of the underlying Co superstructure. We further uncover an apparent tunability of the spin modulations likely due to tilting of the underlying Co moments. Spin tilting could potentially provide an explanation for the unidentified 50 K transition seen by other experiments[37,39]. In the scenario of canted spins, spin canting can in principle break the spatial symmetry mapping between spin-up and spin-down states, which in turn could affect the altermagnetic band splitting since the compensation between spin-sublattices may no longer be present.

It is interesting to note that we observe a partial gap opening at the Fermi level (Fig. 3i) that is not predicted by DFT simulations that consider

$Co_{0.25}NbSe_2$ in the altermagnetic state with spins aligned perfectly aligned along the *c*-axis (Fig. 3j). It is conceivable that the spectral gap opening could arise from the magnetic ordering in the 2 × 2 superstructure, but not captured by DFT calculations. Another possibility could be due to a yet to be identified “hidden” order, such as an additional charge, spin or orbital density waves. This will be of high interest to pursue in future experiments and theoretical simulations.

Given the asymmetric response of the density waves dependent on the tip’s spin polarization, the density modulations detected in our experiments also break the time-reversal symmetry. This is further supported by the spin-polarized DOS measurements that show distinct differences for opposite tip spin polarizations (Fig. 3i). In future work, it would be of particular interest to explore the existence and potential control of time-reversal symmetry breaking domains via spin-polarized STM, complementary to the X-ray photoemission electron microscopy domain studies of altermagnetic MnTe thin films[43].

While superconductivity is not detected in our samples, the parent system 2*H*-$NbSe_2$ without Co intercalation is a well-known bulk superconductor with $\sim 3a_0 \times 3a_0$ charge density wave state. Therefore, it would be of particular interest to explore how undoped 2*H*-$NbSe_2$ evolves into a non-superconducting altermagnet at $x = 1/4$ Co concentration by studying a range of intermediate Co concentrations. It is conceivable that intercalation of a smaller density of Co atoms, or intercalating a different magnetic element altogether, could stabilize both superconductivity and altermagnetism in the same compound, providing a unique platform to study the interplay of superconductivity and altermagnetism, potentially generating unconventional Cooper pair density waves[44]. In general, intercalating transition metal dichalcogenides can provide a widely tunable platform to realize new materials systems, in the search for novel correlated electronic states in altermagnets.

Methods

Sample growth

Single crystals of $Co_{0.25}NbSe_2$ were grown via the chemical vapor transport. High-purity powders of cobalt (Co, 99.99%), niobium (Nb, 99.999%), and selenium (Se, 99.9999%) were used as starting materials. To minimize contamination and residual oxygen, the quartz ampoule underwent thorough chemical cleaning and vacuum heat treatment before loading the reactants. The precursor materials were then sealed inside a quartz ampoule (~10 mm in diameter and 150 mm in length) along with iodine (5 mg/cm^3 relative to ampoule volume) as a transport agent. After being evacuated to high vacuum, the sealed ampoule was placed in a two-zone horizontal furnace, with the source region maintained at a higher temperature than the deposition zone. Achieving high-quality crystal growth required precise control of the temperature gradient and iodine concentration. For Co0.25NbSe$_2$, the source region was maintained at 960–980 °C, while the growth region temperature was systematically increased from 880 to 900 °C over 100 h. The system was then held at these temperatures for an additional 300 h to enable the formation of large single crystals. Finally, a controlled cooling process was implemented over 100 h, lowering the source region to 200 °C and the growth region to 100 °C before allowing the ampoule to reach room temperature naturally. The obtained crystals had typical dimensions of ~5 × 5 × 0.1 mm^3. Residual iodine was removed by rinsing the crystals with a methanol solution. The composition was preliminarily assessed via energy-dispersive X-ray spectroscopy using a field-emission scanning electron microscope (FE-SEM, JEOL 7500).

STM experiments

Samples were glued to the sample holder using EPO-TEK H20E silver conducting epoxy and cured at 175 °C for 20 min. The cleaving rod was then glued to the top of the sample in the same way. We cold-cleaved the crystals in UHV at a cryogenic temperature (approximately few tens of Kelvin) and quickly inserted them into the STM head for scanning. STM data was acquired using a customized Unisoku USM1300 microscope. The STM tips used were homemade, chemically-etched tungsten tips, annealed in UHV to bright orange color prior to STM experiments. For preparing a spin-polarized tip, the tip scanned and bias-pulsed over the sample, which gave rise to the tip picking up Co adatoms and becoming spin-polarized. After acquiring data with the spin-polarized tip, its spin polarization was characterized by scanning on a UHV-cleaved surface of FeTe (see Supplementary Fig. 6), an antiferromagnet with a well-defined bicollinear AFM ordering on the surface. By this, we found that typical spin-polarized tips are ferromagnetic-like (i.e., change their polarization direction with different directions of magnetic field). Unless otherwise specified, STM measurements were taken at about 4.8 K.

STM analysis

To read out the intensity of the 2 × 2 peaks in the Fourier transform, the Lawler–Fujita drift-correction algorithm was applied to our topographs and DOS maps[45]. This algorithm shifts and crops the original image so that the atomic Bragg peaks are single pixel and even integer coordinates in Fourier space, thus minimizing artificial effects from piezo and thermal drift. Since the 2 × 2 peaks are a multiple of the lattice constant, these too are shifted to single pixels for intensity read-out.

ARPES experiments

The ARPES data (Supplementary Fig. 11) were obtained at the CASSIOPÉE beamline of Synchrotron SOLEIL (France) using linearly horizontal polarized light with 70 eV and 25 eV photon energies. The Fermi surfaces were integrated ±15 meV from the Fermi level. The samples were cleaved in UHV at a pressure better than 3×10^{-10} mbar, and the spectra were collected with a Scienta R4000 analyzer with momentum and energy resolution better than 0.018 Å^{-1} and 10 meV, respectively.

DFT calculations

DFT calculations have been performed in the collinear spin-polarized configuration and via the plane-wave pseudopotential method, as implemented in the Quantum ESPRESSO package[46,47]. Electron-ion interaction has been modeled for Se atoms via a norm-conserving pseudopotential, while for Nb and Co atoms via ultrasoft pseudopotentials: we chose an energy cut-off of 45 Ry and 450 Ry for the wave-function and electron density, respectively.

Electronic band structure for the bulk Co-doped 2 × 2 $NbSe_2$ supercell in the altermagnetic phase has been obtained through Perdew–Burke–Ernzerhof[48] exchange-correlation functional, sampling the Brillouin zone with a *k*-vector mesh of 9 × 9 × 16 points and a first-order Methfessel–Paxton[49] electronic smearing of 5 mRy. Electronic dispersion has then been mapped into the large Brillouin zone of undoped 1 × 1 $NbSe_2$ via an unfolding procedure[50] implemented in the code unfold.x[51].

The electronic DOS projected on the Se atoms was then calculated for the surface, employing a slab geometry consisting of 5 layers of 2*H*-$NbSe_2$ and four Co atoms. In order to properly simulate a 2D system we added 20 Å of vacuum in the non-periodic direction orthogonal to the surface. Ground-state electronic density was then obtained via a *k*-vector mesh of 9 × 9 × 1 points and a first-order Methfessel–Paxton[49] electronic smearing of 5 mRy, while DOS has been computed with a *k*-vector mesh of 54 × 54 × 1 points and a Gaussian electronic smearing of 0.25 mRy.

STM images at constant height (3 Å from the surface) have been obtained by integrating the DOS from the bias potential to the Fermi energy, as proposed by Tersoff and Hamann[52].

Data availability

Data supporting the findings of this study are available via Zenodo at https://zenodo.org/records/18001533and upon request from the corresponding author. Source data are provided with this paper.

Code availability

The code that supports the findings of the study is available from the corresponding authors upon reasonable request.

Received: 24 November 2025; Accepted: 12 January 2026;

References

1. Hayami, S., Yanagi, Y. & Kusunose, H. Momentum-dependent spin splitting by collinear antiferromagnetic ordering. *J. Phys. Soc. Jpn.* **88**, 123702 (2019).
2. Šmejkal, L., González-Hernández, R., Jungwirth, T. & Sinova, J. Crystal time-reversal symmetry breaking and spontaneous Hall effect in collinear antiferromagnets. *Sci. Adv.* **6**, eaaz8809 (2020).
3. Yuan, L.-D., Wang, Z., Luo, J.-W., Rashba, E. I. & Zunger, A. Giant momentum-dependent spin splitting in centrosymmetric low-*z* antiferromagnets. *Phys. Rev. B* **102**, 014422 (2020).
4. Mazin, I., Koepernik, K., Johannes, M. D., González-Hernández, R. & Šmejkal, L. Prediction of unconventional magnetism in doped $FeSb_2$. *Proc. Natl. Acad. Sci. USA* **118**, e2108924118 (2021).
5. Šmejkal, L., Sinova, J. & Jungwirth, T. Emerging research landscape of altermagnetism. *Phys. Rev. X* **12**, 040501 (2022).
6. Šmejkal, L., Sinova, J. & Jungwirth, T. Beyond conventional ferromagnetism and antiferromagnetism: a phase with nonrelativistic spin and crystal rotation symmetry. *Phys. Rev. X* **12**, 031042 (2022).
7. Mazin, I. Editorial: Altermagnetism—a new punch line of fundamental magnetism. *Phys. Rev. X* **12**, 040002 (2022).
8. Šmejkal, L., Hellenes, A. B., González-Hernández, R., Sinova, J. & Jungwirth, T. Giant and tunneling magnetoresistance in unconventional collinear antiferromagnets with nonrelativistic spin-momentum coupling. *Phys. Rev. X* **12**, 011028 (2022).
9. González-Hernández, R. et al. Efficient electrical spin splitter based on nonrelativistic collinear antiferromagnetism. *Phys. Rev. Lett.* **126**, 127701 (2021).
10. Feng, Z. et al. An anomalous Hall effect in altermagnetic ruthenium dioxide. *Nat. Electron.* **5**, 735–743 (2022).
11. Bai, H. et al. Observation of spin splitting torque in a collinear antiferromagnet RuO_2. *Phys. Rev. Lett.* **128**, 197202 (2022).
12. Karube, S. et al. Observation of spin-splitter torque in collinear antiferromagnetic RuO_2. *Phys. Rev. Lett.* **129**, 137201 (2022).
13. Bose, A. et al. Tilted spin current generated by the collinear antiferromagnet ruthenium dioxide. *Nat. Electron.* **5**, 267 (2022).
14. Tschirner, T. et al. Saturation of the anomalous Hall effect at high magnetic fields in altermagnetic RuO_2. *APL Mater.* **11**, 101103 (2023).
15. Wang, M. et al. Emergent zero-field anomalous Hall effect in a reconstructed rutile antiferromagnetic metal. *Nat. Commun.* **14**, 8240 (2023).
16. Guo, Y. et al. Direct and inverse spin splitting effects in altermagnetic RuO_2. *Adv. Sci*. **11**, https://doi.org/10.1002/advs.202400967 (2024).
17. Wang, Z. Q. et al. Inverse spin hall effect dominated spin-charge conversion in (101) and (110)-oriented RuO_2 films. *Phys. Rev. Lett.* **133**, 046701 (2024).
18. Osumi, T. et al. Spin-degenerate bulk bands and topological surface states of RuO_2. Preprint at https://arxiv.org/abs/2501.10649 (2025).
19. Keßler, P. et al. Absence of magnetic order in RuO_2: insights from μsr spectroscopy and neutron diffraction. Preprint at https://arxiv.org/abs/2405.10820 (2024).
20. Hiraishi, M. et al. Nonmagnetic ground state in RuO_2 revealed by muon spin rotation. *Phys. Rev. Lett.* **132**, 166702 (2024).
21. Fedchenko, O. et al. Observation of time-reversal symmetry breaking in the band structure of altermagnetic RuO_2. *Sci. Adv.* **10**, eadj4883 (2024).
22. Krempaský, J. et al. Altermagnetic lifting of kramers spin degeneracy. *Nature* **626**, 517–522 (2024).
23. Lee, S. et al. Broken kramers degeneracy in altermagnetic MnTe. *Phys. Rev. Lett.* **132**, 036702 (2024).
24. Osumi, T. et al. Observation of a giant band splitting in altermagnetic MnTe. *Phys. Rev. B* **109**, 115102 (2024).
25. Gonzalez Betancourt, R. D. et al. Spontaneous anomalous hall effect arising from an unconventional compensated magnetic phase in a semiconductor. *Phys. Rev. Lett.* **130**, 036702 (2023).
26. Kluczyk, K. P. et al. Coexistence of anomalous hall effect and weak magnetization in a nominally collinear antiferromagnet MnTe. *Phys. Rev. B* **110**, 155201 (2024).
27. Betancourt, R. D. G. et al. Anisotropic magnetoresistance in altermagnetic MnTe. *npj Spintronics* **2**, https://www.nature.com/articles/s44306-024-00046-z#citeas (2024).
28. Hariki, A. et al. X-ray magnetic circular dichroism in altermagnetic MnTe. *Phys. Rev. Lett.* **132**, 176701 (2024).
29. Liu, Z., Ozeki, M., Asai, S., Itoh, S. & Masuda, T. Chiral split magnon in altermagnetic MnTe. *Phys. Rev. Lett.* **133**, 156702 (2024).
30. Han, L. et al. Electrical 180°) switching of néel vector in spin-splitting antiferromagnet. *Sci. Adv.* **10**, eadn0479 (2024).
31. Reichlova, H. et al. Observation of a spontaneous anomalous hall response in the Mn_5Si_3 d-wave altermagnet candidate. *Nat. Commun.* **15**, 4961 (2024).
32. Biniskos, N. et al. Complex magnetic structure and spin waves of the noncollinear antiferromagnet Mn_5Si_3. *Phys. Rev. B* **105**, 104404 (2022).
33. Nakatsuji, S., Kiyohara, N. & Higo, T. Large anomalous hall effect in a non-collinear antiferromagnet at room temperature. *Nature* **527**, 212–215 (2015).
34. Reimers, S. et al. Direct observation of altermagnetic band splitting in CrSb thin films. *Nat. Commun.* **15**, 2116 (2024).
35. Ghimire, N. J. et al. Large anomalous Hall effect in the chiral-lattice antiferromagnet $CoNb_3S_6$. *Nat. Commun.* **9**, 3280 (2018).
36. Jiang, B. et al. Discovery of a metallic room-temperature d-wave altermagnet KV_2Se_2O. *Nat. Phys*. **21**, 754 (2025).
37. Regmi, R. B. et al. Altermagnetism in the layered intercalated transition metal dichalcogenide $CoNb_4Se_8$. *Nat. Commun.* **16**, 4399 (2025).
38. Dale, N. et al. Non-relativistic spin splitting above and below the fermi level in a *g*-wave altermagnet. Preprint at https://arxiv.org/abs/2411.18761 (2024).
39. Vita, A. D. et al. Optical switching in a layered altermagnet. Preprint at https://arxiv.org/abs/2502.20010 (2025).
40. Moncton, D. E., Axe, J. D. & DiSalvo, F. J. Study of superlattice formation in 2H-$NbSe_2$ and 2H-$TaSe_2$ by neutron scattering. *Phys. Rev. Lett.* **34**, 734–737 (1975).
41. Giambattista, B., Johnson, A., Coleman, R. V., Drake, B. & Hansma, P. K. Charge-density waves observed at 4.2 k by scanning-tunneling microscopy. *Phys. Rev. B* **37**, 2741–2744 (1988).
42. Hess, H. F., Robinson, R. B., Dynes, R. C., Valles, J. M. & Waszczak, J. V. Scanning-tunneling-microscope observation of the Abrikosov flux lattice and the density of states near and inside a fluxoid. *Phys. Rev. Lett.* **62**, 214–216 (1989).
43. Amin, O. J. et al. Nanoscale imaging and control of altermagnetism in MnTe. *Nature* **636**, 348–353 (2024).
44. Parthenios, N. et al. Spin and pair density waves in 2d altermagnetic metals. *Phys. Rev. B*. **112**, 214410 (2025).
45. Lawler, M. J. et al. Intra-unit-cell electronic nematicity of the high-tc copper-oxide pseudogap states. *Nature* **466**, 347–351 (2010).
46. Giannozzi, P. et al. Quantum espresso: a modular and open-source software project for quantum simulations of materials. *J. Phys. Condens. Matter* **21**, 395502 (19pp) (2009).
47. Giannozzi, P. et al. Advanced capabilities for materials modelling with Quantum Espresso. *J. Phys. Condens. Matter* **29**, 465901 (2017).

48. Perdew, J. P., Burke, K. & Ernzerhof, M. Generalized gradient approximation made simple. *Phys. Rev. Lett.* **77**, 3865–3868 (1996).
49. Methfessel, M. & Paxton, A. T. High-precision sampling for Brillouin-zone integration in metals. *Phys. Rev. B* **40**, 3616–3621 (1989).
50. Popescu, V. & Zunger, A. Extracting E versus $\vec{k}$ effective band structure from supercell calculations on alloys and impurities. *Phys. Rev. B* **85**, 085201 (2012).
51. Pacilè, D. et al. Narrowing of d bands of FeCo layers intercalated under graphene. *Appl. Phys. Lett.* **118**, 121602 (2021).
52. Tersoff, J. & Hamann, D. R. Theory of the scanning tunneling microscope. *Phys. Rev. B* **31**, 805 (1985).

Acknowledgements

I.Z. gratefully acknowledges the support from the US Department of Energy grant number DE-SC0025005. F.Ma. greatly acknowledges the NFFA-DI funded by the European Union - NextGenerationEU, M4C2, within the PNRR project NFFA-DI, CUP B53C22004310006, IR0000015. Z.W. acknowledges the support of U.S. Department of Energy, Basic Energy Sciences Grant No. DE-FG02-99ER45747. M.B.P. and J.A.M gratefully acknowledge support from DanScatt (7129-00018B). D.R. acknowledges support from the HPC resources of IDRIS, CINES, and TGCC under Allocation No. 2024-A0160914101 made by GENCI. Y.H. acknowledges the support from the National Research Foundation of Korea (NRF) grant funded by the Korea government (MSIT) (NRF-2022R1I1A1A01063507 and RS-2025-24742993). F.Mo. acknowledges funding from the European Union's Horizon 2020 Research and Innovation Programme under Project SINFONIA, Grant n. 964396. A.D.V. acknowledges the Deutsche Forschungsgemeinschaft (DFG) within Transregio TRR 227 Ultrafast Spin Dynamics project B07, the Max Planck Society, and BERLIN QUANTUM, an initiative endowed by the Innovation Promotion Fund of the city of Berlin.

Author contributions

C.C. performed STM measurements with the help from M.X., S.C., and A.L. F.M., A.D.V., M.B.P., C.B., and J.A.M. collected the ARPES data. M.C. and D.R. performed the DFT calculations. W.A.C. helped with magnetization measurements. G.V., F.Mo. and P.O. performed additional sample characterization via XRD and XPS. Y.H. synthesized the bulk single crystals. Z.W. provided a theoretical input on the experimental analysis. I.Z., C.C., and F.Ma. wrote the paper with the input from all the authors. I.Z. supervised the project.

Competing interests

The authors declare no competing interests.

Additional information

Supplementary information The online version contains supplementary material available at https://doi.org/10.1038/s43246-026-01081-5.

Correspondence and requests for materials should be addressed to Younghun Hwang, Federico Mazzola or Ilija Zeljkovic.

Peer review information *Communications Materials* thanks the anonymous reviewers for their contribution to the peer review of this work. A peer review file is available.